Materials Science-Poland
Volume 43 Issue 4 · pp. 134–150 · DOI: 10.2478/msp-2025-0046

Materials Science-Poland

Experimental and first-principles investigation of high entropy superalloys produced by powder injection moulding method

Research Article

Emre Atakan Meric, Berke Soy, Ilven Mutlu*

Department of Metallurgical and Materials Engineering, Istanbul University-Cerrahpasa, Istanbul, 34320, Turkey

Received 05 June 2025; Accepted 16 December 2025

Abstract: In this study, AlCoCrFeMnNiTi based refractory-free high entropy superalloys (HESA) were prepared by powder injection moulding (PIM) for aviation applications. Aging was done in order to enhance mechanical properties. Ni-based superalloys are expensive and heavy due to expensive alloying elements with high density. Strength, oxidation and creep resistance of the high entropy alloys are low for engine applications. HESA would be cheaper and lighter than superalloys and would have higher strength, creep resistance and oxidation resistance than high entropy alloys. In order to obtain solid solution, mixing entropy and mixing enthalpy values were adjusted. Valance electron concentrations was adjusted in order to obtain face centered cubic structure. There is grain-coarseing and segregation in HESA produced by vacuum arc melting. HESA with finer grain sizes and low segregation could be produced by using mechanical alloying (MA)-PIM. Alloy powders were prepared by MA. Alloys with high solid solubility, complex shaped, fine grained superalloy specimens were produced by MA-PIM. Polymer binder consisted polyethylene, paraffin, and stearic acid. Feedstock consisted of 45% of binder and 55% of alloy powder. PIM was carried out at 185°C. After the PIM, binder was removed by chemical debinding and thermal debinding. Sintering was carried out at 1,250°C. Elevated temperature properties of the HESA was enhanced by intermetallic precipitates which were obtained by alloying and heat treatments. Corrosion properties, high temperature oxidation properties, thermal properties, mechanical properties were determined.

Keywords: *Superalloys • High entropy • Aircraft • Heat treatment • Powder injection moulding*

1. Introduction

High-temperature aircraft engine applications require alloys having low density, oxidation resistance, corrosion resistance, strength and creep resistance. Ni-based superalloys are the most common materials for jet engine parts. Main problems of the superalloys are their relatively high cost and high density. Industrial superalloys, such as Ni-based Inconel 718 and Ni-based Inconel 625, consist of face centered cubic (γ) matrix and some Ni_3Ti or/and Ni_3Al (γ') precipitates, which enhance the strength of the face centered cubic (γ) matrix [1–15].

High entropy alloys are novel materials and have potential for the aircraft engine applications. High entropy alloys have 5–13 principle elements in near-equal atomic contents and tend to forma a solid-solution. Mixing entropy reaches a high value when the alloying elements are in equal compositions, and this high entropy leads to solid solution formation instead of brittle intermetallic compounds. High entropy alloys main effects are sluggish-diffusion, high-entropy, cocktail effect, severe lattice distortion. In addition, entropy of mixing, valence electron concentration, atomic diameter differences, melting temperatures, and mixing enthalpy values are useful for microstructure prediction in the high entropy alloys. Chen et al. [9] were investigated the effect of valance electron concentration (VEC) on the strength and ductility of the high entropy alloys. High VEC values produced face centered cubic (fcc) lattice structure with high ductility, while low VEC values produced body centered cubic (bcc) lattice structure with low ductility and high strength. Al and Cr additions enhanced the stability of body centered cubic phase, while Ni and Co alloying enhanced the stability of

* *E-mail: imutlu@istanbul.edu.tr*

face centered cubic phase. The authors found that, VEC, higher than 8.0 produced fcc structure, while VEC lower than 6.8 produced bcc structure.

High temperature mechanical properties of the high entropy alloys are not strong enough for engine applications. Alternative strengthening methods, such as aging, must be employed in order to enhance the mechanical properties. At high temperatures in jet engine working conditions, diffusion induced phase transformation and creep must be prevented. In general, face centered cubic phase with lower diffusion rate than the body centered cubic phase must used at elevated temperatures. As industrial Ni-based superalloys consist of (γ^I) precipitates in face centered cubic (γ) matrix for creep resistance, same microstructure, (γ^I) precipitates in fcc (γ) matrix should be formed in the high entropy alloys. However, amount of the γ^I phase (precipitates) should be controlled by the increase in the mixing entropy. So, Ni composition of the high entropy alloy should be 35% or higher. As the Ni contents and microstructures of the Ni-reach high entropy alloy are close to industrial Ni-based superalloys, this alloys could be defined as high entropy superalloys (HESA). High-entropy superalloy joins the high entropy alloys with the superalloys in order to develops novel elevated temperature material. Yeh et al. [1] prodeced HESA for high temperature applications with higher Fe and Ti contents than superalloys. Lower price and lower density values were obtained than than industrial superalloys. The HESA specimens were produced by vacuum arc melting method. Jones et al. [2] produced and investigated refractory HESA. Microstructure of the specimens consisted of bcc matrix and B2 precipitates. $AlMo_{0.5}NbTa_{0.5}TiZr$ (20Al-10Mo-20Nb-10Ta-20Ti-20Zr) refractory HESA specimens were produced bu vacuum arc melting method. Tsai et al. [3] studied the high temperature oxidation mechanism of AlCoCrFeNiTiNb based HESA produced by vacuum arc melting. Nb addition increased the oxitadion resistance. Its found that, the Nb addition encreased the oxidation resistnce. Senkov et al. [4] produced $AlMo_{0.5}NbTa_{0.5}TiZr_{0.5}$, $AlNbTa_{0.5}TiZr_{0.5}$, $Al_{0.5}Mo_{0.5}NbTa_{0.5}TiZr$ and $Al_{0.25}NbTaTiZr$ refractory HESA by vacuum arc melting. Nili-Ahmadabadi et al. [5] produced precipitation hardenable HESA by double vacuum melting. Microstructure was investigated after homogenization, hor rolling, annealing and aging. Aging was studied with solutionizing and without solutionizing. Mechanical properties of the direct aged specimens were higher than solutionized-aged specimens. Yurchenko et al. [6] investigated $Nb_{30}Mo_{30}Ti_{20}Co_{20}$ refractory HESA specimens. The specimens were supplied as a rod, which was produced by vacuum casting method. Solutionizing heat treatment at 1,200°C temperature provided semi-coherent Co-based and Ti-based B2 precipitates, and fcc Ti-based precipitates in Nb-based and Mo-based bcc matrix.

Mechanical alloying (MA) includes material transfer (diffusion) in order to obtain a uniform alloy [16,17]. Powder injection molding is a powder metal forming technology used for production of small-medium sizes complex products. Powder injection molding overcomes the shape limitation of traditional powder metallurgy, productivity of hot isostatic pressing and cold isostatic pressing, cost of machining, and high tolerance of casting. Powder injection molding includes feedstock preparation by blending metal powder and binder, granulation, powder injection molding, debinding, sintering steps. Hong et al. [15] were produced $Ni_{46}Co_{22}Al_{12}Cr_8Fe_8Ti_3Mo_1$ HESA by traditional powder metallurgy. Kim et al. [13] CoCrFeMnNi high entropy alloys were produced by powder injection moulding (PIM). Effect of heating rate on the mechanical properties and segregation was investigated. Gas atomised CoCrFeMnNi powders were used as a raw material. Optimum metal loading was 66%. Meza et al. [14] were produced high entropy alloys by using industrial superalloy powders (Inconel 625). Lattice structure of the high entropy alloy was face centered cubic. Polymer based binder was polyethyleneglycol-cellulose acetate butyrate.

In this study, AlCoCrFeMnNiTi based refractory-free HESA were prepared by PIM for aviation applications. Heat treatment was performed to enhance high temperature mechanical properties. Traditional Ni-based superalloys are expensive and heavy due to expensive alloying elements with high density. Elevated temperature strength, oxidation resistance and creep resistance of the high entropy alloys are low for aviation applications. HESA would be cheaper and lighter than superalloys and would have higher strength, creep resistance and oxidation resistance than high entropy alloys. HESA includes more light elements (Al and Ti), and lesser expensive elements (Co and Ni). Also, there is no heavy and expensive refractory elements (W, Nb, Mo, Ta). There is grain-coarseing, and segregation in HESA produced by vacuum arc melting. HESA with finer grain sizes and low segregation could be produced by using MA-PIM. Although there are studies on the production of HESA by vacuum arc melting or traditional powder metallurgy, there is no study on the production of HESA by PIM. There is no any study on the seven element Al-Co-Cr-Fe-Mn-Ni-Ti high entropy alloy system in the literature.

2. Experimental

2.1 HESA composition design

In the present study Al-Co-Cr-Fe-Mn-Ni-Ti based HESA were produced. Table 1 shows the chemical compositions of the HESA. Al, Co, Cr, Fe, Mn, Ni and Ti elements were

selected due to their melting temperature, electrical conductivity, density, corrosion resistance, mechanical properties, price. Al, Co, Cr, Fe, Mn, Ni and Ti elements were used in the range of 3–38 wt%. Al, Co, Cr, Fe, Mn, Ni, Ti elements were selected in order to develop light, cheap HESAs with creep resistance and strength. HESA includes more light elements (Al and Ti), and lesser expensive elements (Co and Ni). Also, there is no heavy and expensive refractory elements (W, Nb, Mo, Ta).

Entropy of mixing (ΔS_{mix}), enthalpy of mixing (ΔH_{mix}), atomic size misfit (δ), parameter Ω, VEC parameters could be used in order to evaluate high entropy alloy formation. Entropy of mixing (ΔS_{mix}) of the proposed HESAs is calculated by equation (1), where R is the gas constant and C_i is the atomic ratio (molar fraction). There is no any interaction forcess between alloy atoms in the ideal solid solutions. The mixing enhalpy is zero, and the mixing entropy is given by the configurational entropy of the alloying atoms. In addition, interaction forces are insufficient to affect the mixing entropy in the regular solid solution. In the HESAs mixing entropy (ΔS_{mix}) must be in the range of $11 \le \Delta S_{mix} \le 19$ (J/K mol) for solid solution formation rather than intermetallic formation. ΔS_{mix} is the highest for alloys with nearly equal atomic ratios. ΔS_{mix} has vibrational, electronic, configurational, and magnetic components. In the present study, only configurational entropy is considered [18,19].

$$\Delta S_{mix} = -R\sum_{i}^{n} C_i \ln C_i. \quad (1)$$

The atomic size misfit parameter (δ), which estimates the amount of lattice strain in the alloy, is calculated by equation (2), where r_i is the atomic radius. Atomic size misfit (δ) parameter must be in the range of $0 \le \delta \le 8.5$ for solid solution formation. High δ parameter leads distortion in the lattice, by increasing the free energy, which decrease the stability of solid solution [18,19].

$$\delta = \sqrt{\sum_{i}^{n} C_i(1 - r_i/r)^2}. \quad (2)$$

VEC parameter of the HESAs is calculated by equation (3) by using VEC values of atoms. Crystal structure of the alloys can be predicted by VEC value. Crystal structure types are as follows: VEC > 8.00 fcc (face centered cubic), VEC < 6.87 bcc (body centered cubic), 6.87 < VEC < 8.00 fcc-bcc dual phase [8,9,18,19].

$$\mathrm{VEC} = \sum_{i}^{n} C_i(\mathrm{VEC})_i. \quad (3)$$

The enthalpy of mixing (ΔH_{mix}) is calculated by equation (4), where ΔH_{mix} is mixing; and C_i and C_j are the atomic ratios of the ith and jth components. For a binary mixture, ΔH_{mix} is negative if the A and B atoms are attractive to each one. ΔH_{mix} is positive if the atoms are repulsive. Criteria for solid solution is $-10 < \Delta H_{mix} < 5$ (kJ/mol). A high negative ΔH_{mix} increases the likelihood of formation of intermetallics. Positive ΔH_{mix} indicates lower mixing of different atoms in the liquid state, which leads to separation of alloying elements in the solid state. Only if enthalpy of mixing is close to zero alloying elements could be distributed and could form solid solution [18,19].

$$\Delta H_{mix} = \sum_{i<j} 4H_{ij}c_ic_j. \quad (4)$$

Dimensionless stability parameter (Ω) is calculated by using equation (5), where T_m is the melting temperature. $\Omega > 1$ means that the effect of the ΔS_{mix} is greater than ΔH_{mix}, and the high-entropy phase tends to form. Solid solution formation is possible only if $\Omega > 1$ is satisfied [18,19].

$$\Omega = \left(\sum c_i T_{m,i}\right)\frac{(\Delta S_{mix})}{|\Delta H_{mix}|}. \quad (5)$$

	Alloy	Chemical Composition (wt%)						
		Al	Co	Cr	Fe	Mn	Ni	Ti
(1)	$Al_{15}Co_9Cr_{16}Fe_{20}Mn_4Ni_{33}Ti_3$	15	9	16	20	4	33	3
(2)	$Al_{15}Co_4Cr_{16}Fe_{20}Mn_4Ni_{38}Ti_3$	15	4	16	20	4	38	3
(3)	$Al_{20}Co_4Cr_{16}Fe_{20}Mn_4Ni_{33}Ti_3$	20	4	16	20	4	33	3
(4)	$Al_{20}Co_9Cr_{16}Fe_{15}Mn_4Ni_{33}Ti_3$	20	9	16	15	4	33	3
(5)	$Al_{20}Co_9Cr_{11}Fe_{20}Mn_4Ni_{33}Ti_3$	20	9	11	20	4	33	3
(6)	$Al_{24}Co_6Cr_{11}Fe_{23}Mn_3Ni_{30}Ti_3$	24	6	11	23	3	30	3
(7)	$Al_{25}Co_5Cr_{10}Fe_{25}Mn_3Ni_{27}Ti_5$	25	5	10	25	3	27	5

Table 1. Chemical compositions of the HESA.

	Al	Co	Cr	Fe	Mn	Ni	Ti	[Refs.]
Mass Number	26.982	58.933	51.996	55.845	54.938	58.693	47.867	[18,19]
r (nm)	0.1431	0.1251	0.1249	0.1241	0.1350	0.1245	0.1461	[18,19]
T_m (K)	933	1,768	2,180	1,811	1,519	1,728	1,941	[18,19]
VEC	3	9	6	8	7	10	4	[18,19]

Table 2. Parameters of the atoms.

	Al	Co	Cr	Fe	Mn	Ni	Ti
Al	—	−19	−10	−11	−20	−22	−60
Co	−19	—	−4	−1	−5	0	−28
Cr	−10	−4	—	−1	2	−7	−7
Fe	−10	−1	−1	—	0	−2	−17
Mn	−20	−5	2	0	—	−8	−11
Ni	−22	0	−7	2	−8	—	−35
Ti	−60	−28	−7	−17	−11	−35	—

Table 3. Mixing enthalpy values (kJ/mol) of the binary alloys [18,19].

Table 2 shows the parameters of the atoms used in the production of HESA, while Table 3 shows the mixing enthalpy values (kJ/mol) of the binary alloys. In the present study seven HESA were produced. HESA with high VEC value (maximum fcc content) and simultaneously high ΔS_{mix} was preferred. In general, fcc structure is necessary for creep resistance. ΔS_{mix} and δ values of the HESA were similar.

Table 4 shows the thermodynamic parameters calculated by equations (1)–(5). As the VEC value is slightly lower than 8.0 and higher than 6.87 for all alloys, bcc and fcc mixed microstructure is supposed to form. As the VEC values of the the alloys are close to fcc microstructure area mainly fcc phase could be formed in the microstructure. The values of atomic size misfit parameters (δ) are within the range of solid solution formation. The values of enthalpy of mixing (ΔH_{mix}) are within the range of solid solution formation for alloy 1 and alloy 2. Since the system contains seven elements, entropy of mixing (ΔS_{mix}) is higher than threshold. ΔS_{mix} values of alloys 1, 2, 3, 4, 5, 6, and 7 are suitable. The values of stability parameter Ω of alloys are within the range of solid solution formation. As a result, the $Al_{15}Co_9Cr_{16}Fe_{20}Mn_4Ni_{33}Ti_3$ (alloy 1) and $Al_{15}Co_4Cr_{16}Fe_{20}Mn_4Ni_{38}Ti_3$ (alloy 2) were most suitable for their high VEC value (maximum fcc content), high δ, high Ω, suitable ΔH_{mix}, high ΔS_{mix}.

2.2 First principles based density functional theory (DFT) calculations

First-principles calculation was used to study the mechanical properties. Cambridge sequential total energy package (CASTEP) code, which is a first-principles quantum mechanical based code, was used for the calculations [20–29]. CASTEP is a first-principles plane wave pseudopotentials method based on DFT. Generalized gradient approximation of Perdew-Burke-Ernzerhof was employed in order to describe the exchange correlation energy. Vanderbilt type ultrasoft pseudopotential was used. Cut-off energy is set to 500 eV and 8 × 8 × 8 k-points were used for structure optimization. Face centered cubic structure was used for alloys.

HESA	VEC (e/a)	δ (%)	ΔS_{mix} (J/K mol)	ΔH_{mix} (kJ/mol)	Ω
$Al_{15}Co_9Cr_{16}Fe_{20}Mn_4Ni_{33}Ti_3$	7.985	6.79	13.78394	−10.898	2.222
$Al_{15}Co_4Cr_{16}Fe_{20}Mn_4Ni_{38}Ti_3$	8.041	6.79	12.97311	−11.183	2.035
$Al_{20}Co_4Cr_{16}Fe_{20}Mn_4Ni_{33}Ti_3$	7.791	6.77	13.47905	−12.521	1.866
$Al_{20}Co_9Cr_{16}Fe_{15}Mn_4Ni_{33}Ti_3$	7.850	6.74	13.94583	−12.765	1.892
$Al_{20}Co_9Cr_{11}Fe_{20}Mn_4Ni_{33}Ti_3$	7.954	6.74	13.80207	−12.338	1.917
$Al_{24}Co_6Cr_{11}Fe_{23}Mn_3Ni_{30}Ti_3$	7.747	6.70	13.64152	−13.223	1.753
$Al_{25}Co_5Cr_{10}Fe_{25}Mn_3Ni_{27}Ti_5$	7.575	6.67	13.86842	−15.053	1.561

Table 4. Calculated parameters of the AlCoCrFeMnNiTi based HESAs.

2.3 MA

In the present study, seven Al-Co-Cr-Fe-Mn-Ni-Ti based refractory element-free HESA were prepared by MA-PIM. Average particle sizes metal powders were 34 μm. Elemental metal powder mixture was ball-milled (mechanical alloying) with ZrO_2 grinding 6 mmvballs for 35 h at 400 rpm. ZrO_2 to metal ratio was 10/1.

2.4 PIM

Polymer system contained 70% polyethylene, 28% paraffin, 2% stearic acid. Feedstock consisted of 45% of binder and 55% of metal. PIM was carried out at 185°C. After the PIM step, binder from green specimens was removed in hot hexane (chemical debinding). Thermal removal of the binder from the green specimens was carried out in a furnace at 400°C for 60 min (thermal debinding). Sintering process of the brown specimens was carried out at 1,250°C for 60 min in vacuum (MTI, USA). Figure 1 illustrates the HESA production steps by MA-PIM method.

2.5 Precipitation hardening (Aging)

In the present study, heat treatment for production of precipitates consisted of a solution treatment and aging. Solution treatment was carreid out above the solvus temperature at 1,150°C for 8 h for dissolution of alloying elements. Precipitation hardening (aging) was carried out at temperatures between 700 and 1,000°C for 5 h for production of precipitates. Titanum was added to the HESA for the formation of coherent fine intermetallic precipitates. After the solution treatment in the vacuum, alumina tube was removed out from the heating zone and the specimens were quenched. Figure 2 shows the aging heat treatment by using sliding-flange tube furnace.

2.6 Characterisation of mechanical properties

Microstructural characterization of the HESA was performed by scanning electron microscope (SEM). Hardness of the specimens was determined by using a micro-vickers hardness test (Zwick Roell). Wear resistance of the specimens was measured by pin-on-disc method (Devotrans, Turkey). Electrical conductivity was investigated by using eddy current device (WeldCheck). Young's modulus values of the specimens were determined by using ultrasonic device (General Electric, USA), by using following equation (6). V_T and V_L are transverse and longitudinal velocity, and ρ is density [30].

$$E = \rho V_T^2 \frac{3V_L^2 - 4V_T^2}{V_L^2 - V_T^2}. \quad (6)$$

2.7 Electrochemical corrosion and oxidation tests

Electrochemical corrosion tests were carred out using a potentiostat (Interface 1000, Gamry) in 5% NaCl solution.

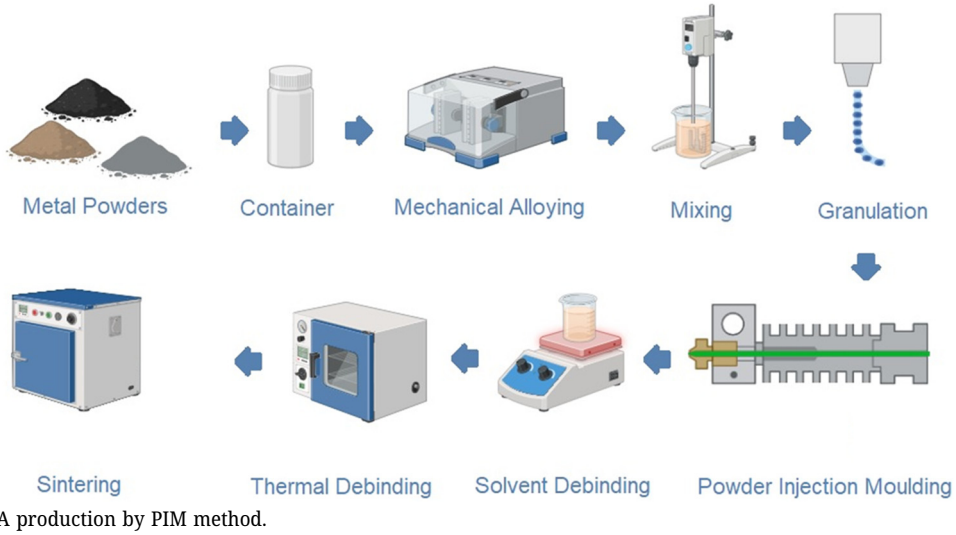

Figure 1. HESA production by PIM method.

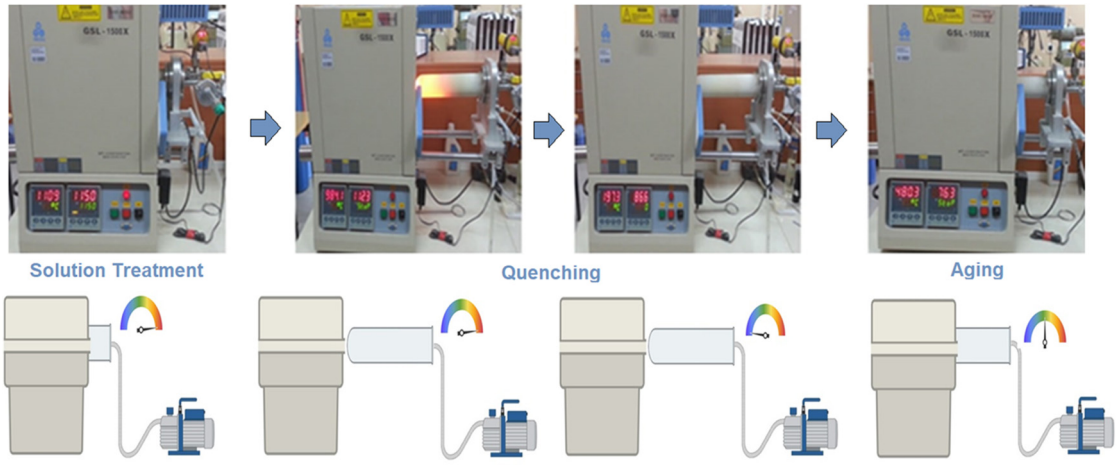

Figure 2. Aging heat treatment by using sliding-flange tube furnace.

Tafel and linear polarization resistance tests were employed for corrosion rate. Electrochemical impedance spectroscopy (EIS) tests were carried out in order to investigate the electrochemical corrosion properties of the HESA specimen and to investigate behaviour of surface. EIS result was fitted by an electrical equivalent circuit model.

Elevated temperature oxidation behaviour of the specimens was studied at 900°C temperature for different durations between 1 and 4 h in air atmosphere. Weight gain values of the specimens were determined by measuring the weight of the specimens before and after the oxidation tests at 900°C in air.

3. Results and discussion

Figure 3 shows the photographs of (a) power injected specimens with varied metal power contents (0, 25, 35, 45, 55%), and (b) sintered specimen. For proper reology, the PIM feedstocks must be produced at 50–60 vol% metal powder and 40–50 vol% polymer binder contents. Lower polymer binder contents lead to micro-cracks, and low fluidity, while higher polymer binder contents lead to shrinkage defects. Injection temperature must be also carefully adjusted. Low injection temperatures lead to high viscosity, which prevents filling of the mould. On the other hand, homoheneous distribution of metal powders can not be obtained at high injection temperatures. Amount of the surface active materials are also important. Zn-stearate or stearic acid based surface active additives decreases the wettbility and the viscosity [31].

Characterization of the structure of the HESA was carried out by using x-ray diffraction (XRD) analysis. Figure 4 shows the XRD patterns of the powders and sintered $Al_{15}Co_4Cr_{16}Fe_{20}Mn_4Ni_{38}Ti_3$ specimen. Peaks in the XRD spectra of the $Al_{15}Co_4Cr_{16}Fe_{20}Mn_4Ni_{38}Ti_3$ HESA is different from the peaks of elemental powders and correspond to a

Figure 3. Photograph of injected specimens with varied metal contents (left), photograph of sintered specimen (right).

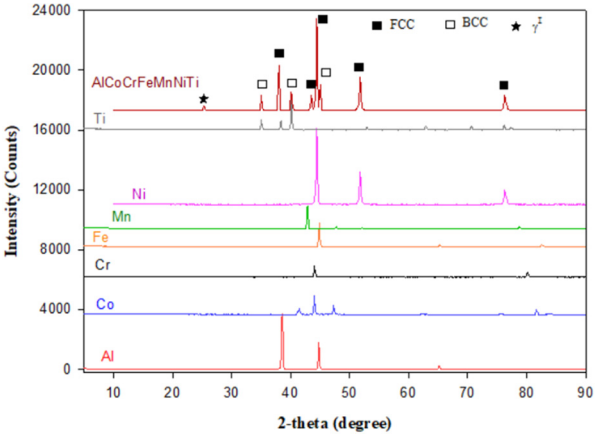

Figure 4. XRD patterns of the elemental powders and sintered HESA.

phase face centered cubic structure, which confirms the formation of a solid solution different from the alloying elements. XRD results showed formation of a matrix phases having face centered cubic structure. Diffraction peaks of body centered cubic phase was also observed, which was arrtibuted to the formation of some body centered cubic phase structure.

Figure 5 shows the XRD patterns of the as-sintered, solution-treated, and aged $Al_{15}Co_4Cr_{16}Fe_{20}Mn_4Ni_{38}Ti_3$ specimen. Diffraction peaks of the body centered cubic (bcc) phase was higher in the solution-treated specimen than the as-sintered specimen. Diffraction peak of the precipitates (γ') was observed in the aged specimen, while diffraction peak of the γ' not observed in the as-sintered and solution treated specimens, which confirms the formation of precipitates after aging (precipitation hardening) heat treatment.

Figure 6 shows the SEM pictures and EDS spectra of the as-sintered, solution treated, and aged (precipitation hardened) $Al_{15}Co_4Cr_{16}Fe_{20}Mn_4Ni_{38}Ti_3$ HESA specimen. As seen from the SEM pictures, microstructure of the solution treated specimen is more homogeneous than as-sintered specimen and aged specimen. As seen from SEM pictures, there is a suitable sintering between the metal particles. Moreover, there is no any microcracks or pores in the microstructure of the aged HESA specimen. EDS spectra of the $Al_{15}Co_4Cr_{16}Fe_{20}Mn_4Ni_{38}Ti_3$ HESA specimen confirms the chemical composition without oxidation.

Figure 7 shows the optic microscope picture of the aged $Al_{15}Co_4Cr_{16}Fe_{20}Mn_4Ni_{38}Ti_3$ HESA specimen. Microstructure of the HESA specimens consist of gamma (γ) phase matrix and some γ' phase intermetallic precipitates. In addition, some body centered cubic phase was also observed. There is no grain-coarseing, and segregation in the microstructure.

Figure 8 shows the effect of (a) heat treatment on the $Al_{15}Co_4Cr_{16}Fe_{20}Mn_4Ni_{38}Ti_3$ alloy and composition (alloy

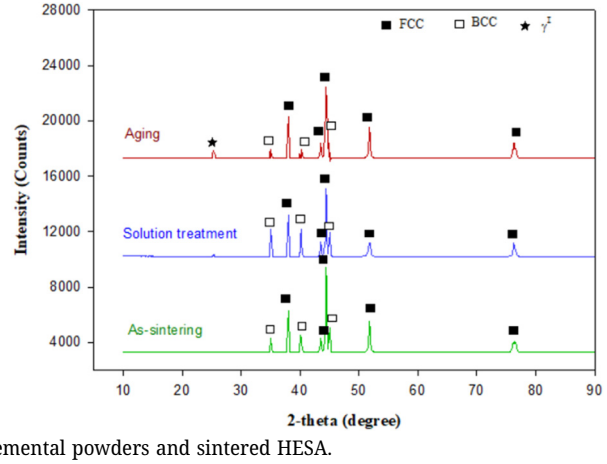

Figure 5. XRD patterns of the elemental powders and sintered HESA.

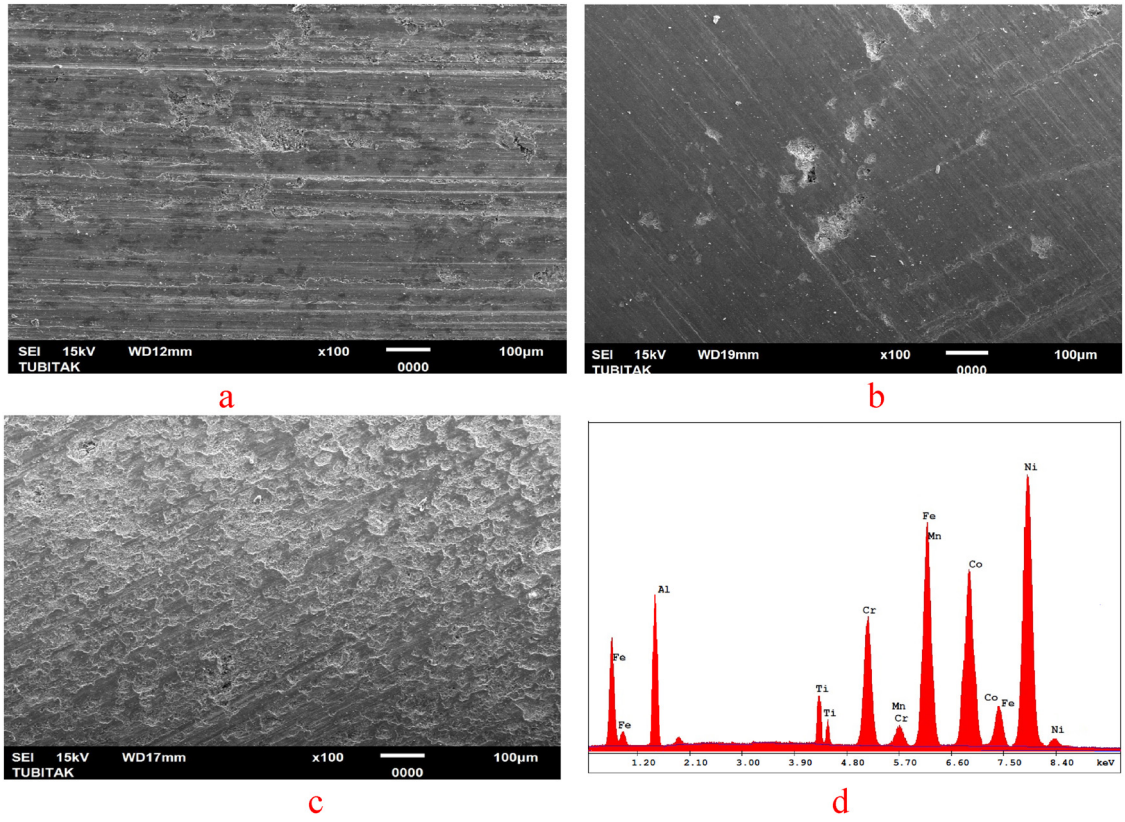

Figure 6. (a) SEM of as-sintered specimen, (b) SEM of solution treated specimen, (c) SEM of aged specimen, (d) EDS of aged specimen.

type) on the Tafel curves. Solution treatment increased the corrosion rate of the as-sintered specimen. Precipitation hardening (aging) at 700 and 1,000°C temperatures was slightly increased the corrosion rate (current density) of the specimens. Maximum corrosion rate was obtained at 1,000°C aging, which was attributed to the formation of large precipitates lead to micro galvanic cells. Corrosion rate value of the specimens aged at 800 and 900°C was close to corrosion rate value of the solution treated specimen.

Equivalent electric circuit model was employed in order to analyse the EIS results. The equivalent electric circuit model includes a barrier-like surface oxide film and metal/oxide film interface. R_{sol} represents resistance of environment (NaCl solution). R_1 and R_2 are polarization resistances (charge transfer resistance) of the oxide and

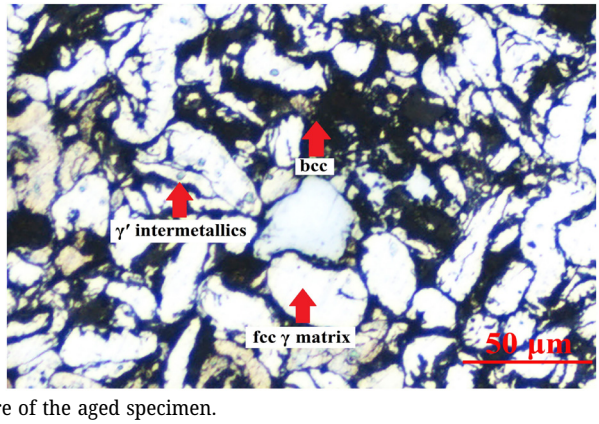

Figure 7. Optic microscope picture of the aged specimen.

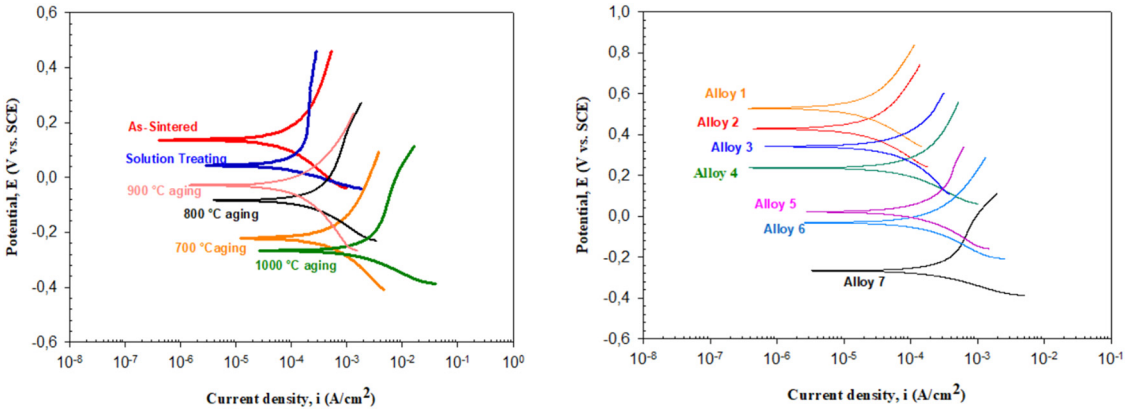

Figure 8. Effect of heat treatment (left), and composition on the Tafel curves (right).

interface. C_1 and C_2 are capacitances (double layer formation) of oxide and interface. Figure 9 shows the EIS results (Nyquist plots). Corrosion resistance (surface oxide film resistance) of alloy 1 and alloy 2 were higher. Highest surface oxide film corrosion resistance was in alloy 1, while lowest was in alloy 7.

Figure 10 shows the (a) effect of heat treatment on the Young's modulus of the $Al_{15}Co_4Cr_{16}Fe_{20}Mn_4Ni_{38}Ti_3$ alloy specimens and (b) effect of composition on the Young's modulus. In general, Young's modulus values of the as-sintered, solution treated and precipitation hardened specimens were close to each other. Young's modulus of the specimen aget at 900°C was slightly higher. Young's modulus values of alloy 1 and alloy 2 were higher. Highest Young's modulus was in alloy 1, while lowest Young's modulus value was in alloy 3.

Figure 11 shows the (a) effect of heat treatment on the wear and (b) effect of composition on the wear. Solution treatment was slighly increased the wear resistance of the as-sintered psecimen. Aging at 700 and 1,000°C temperatures was slightly increased the wear resistance of the solution hardened specimens. Minimum wear was obtained at 900°C aging, which was attributed to the maximum hardness and formation of precipitates having optimum size. Wear value of the specimens aged at 800 and 900°C was close to wear value of the solution treated specimen. Wear values of alloy 1 and alloy 2 were lower. Highest wear value was in alloy 3, while lowest wear (highest wear resistance) was in alloy 1.

Figure 12 shows (a) the effect of heat treatment on the electrical conductivity and (b) effect of composition on the electrical conductivity. Precipitation hardening was decreased the electrical conductivity of the solution hardened specimens. Minimum electrical conductivity was obtained at 1,000°C aging, which was attributed to the maximum hardness and formation of large precipitates. Electrical conductivity values of alloy 6 and alloy 7 were higher. Highest

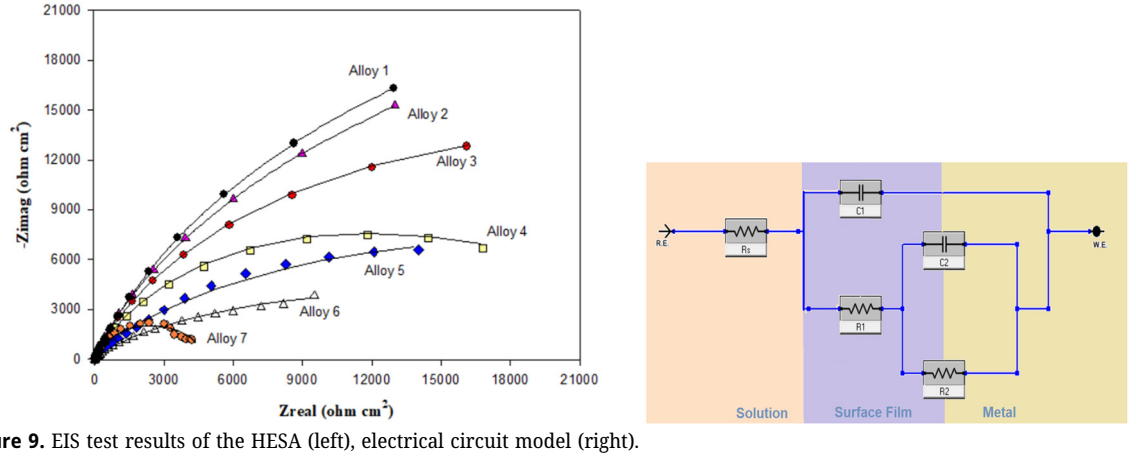

Figure 9. EIS test results of the HESA (left), electrical circuit model (right).

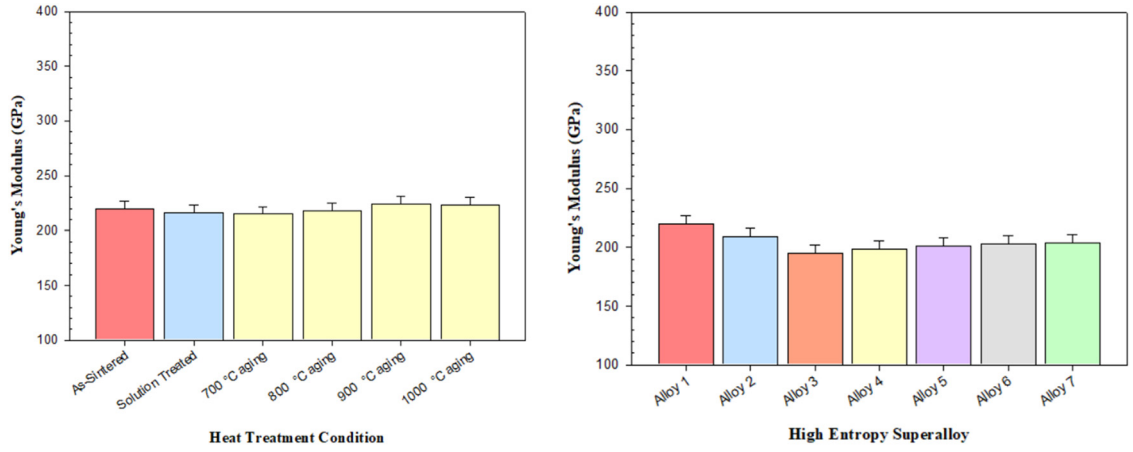

Figure 10. Effect of heat treatment (left), and composition on the Young's modulus of the specimen (right).

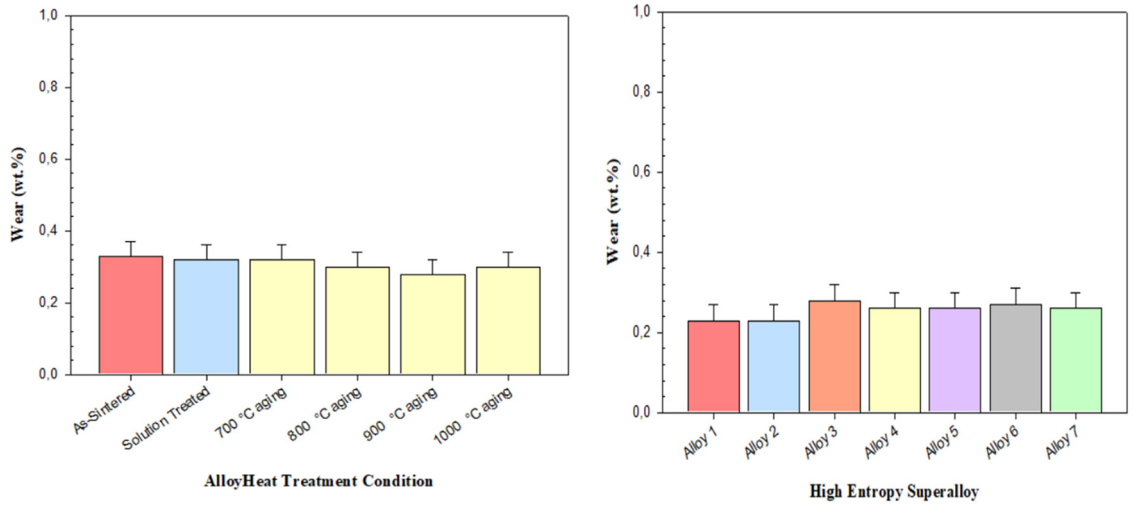

Figure 11. Effect of heat treatment (left), and composition on the wear of the specimens (right).

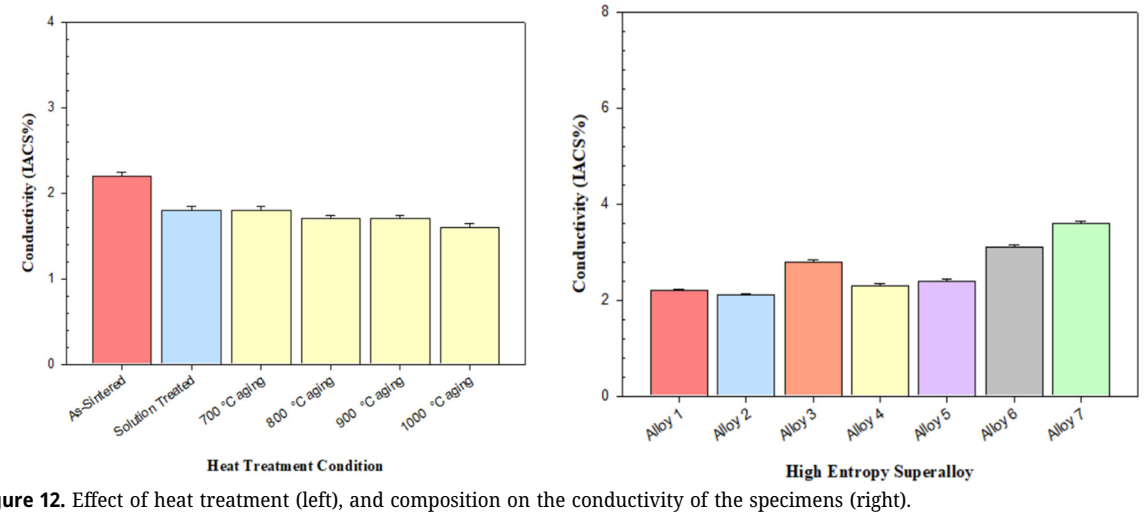

Figure 12. Effect of heat treatment (left), and composition on the conductivity of the specimens (right).

	Alloy	Tensile strength (MPa)
(1)	$Al_{15}Co_9Cr_{16}Fe_{20}Mn_4Ni_{33}Ti_3$	765
(2)	$Al_{15}Co_4Cr_{16}Fe_{20}Mn_4Ni_{38}Ti_3$	742
(3)	$Al_{20}Co_4Cr_{16}Fe_{20}Mn_4Ni_{33}Ti_3$	680
(4)	$Al_{20}Co_9Cr_{16}Fe_{15}Mn_4Ni_{33}Ti_3$	685
(5)	$Al_{20}Co_9Cr_{11}Fe_{20}Mn_4Ni_{33}Ti_3$	690
(6)	$Al_{24}Co_6Cr_{11}Fe_{23}Mn_3Ni_{30}Ti_3$	690
(7)	$Al_{25}Co_5Cr_{10}Fe_{25}Mn_3Ni_{27}Ti_5$	699
Reference	Inconel 718 (NiCr19Fe19Nb5Mo3)	1,050

Table 5. Strength values of the HESA.

electrical conductivity value was in te alloy 7, while lowest electrical conductivity value was in alloy 2.

Table 5 shows the tensile strength values of the HESA. Table 5 also shows the tensile strength value of the traditional Ni-based superalloy (Inconel 718). The results of the HESA have been compared with traditional Ni-Based superalloys. As seen from the Table 5, tensile strength values of the HESA were 27–35% lower than traditional Ni-based superalloy (Inconel 718).

3.1 First principles calculations

In the present study, first-principles based computational materials science calculations were used in order to study the elastic, physical and mechanical properties. CASTEP software, which is a DFT based code, was used for the calculations. Initially, CASTEP geometry optimization process was carried out by decreasing the magnitude of forces up to they become lower than a defined tolerance value. Figure 13 shows the (a) unit cell and (b) superlattice.

Elastic constants should satisfy the mechanical stability criteria for a stable alloy. C_{11}, C_{12} and C_{44} are the independent elastic constants for the simple cubic crystal structures. C_{11}, C_{12} and C_{44} elastic constants must satisfy the following conditions for mechanical stability according to the Born-Huan criteria [20–29]. Figure 14 shows the elastic constants of the alloys. C^I value must be positive for mechanically stability of the crystal structure. As shown in the Figure 14, C^I values are positive and equations (7)–(10) were satisfied, which means all the alloys are mechanically stable.

$$C^I = \frac{(C_{11} - C_{12})}{2}, \tag{7}$$

$$C_{11} + 2C_{12} > 0, \tag{8}$$

$$C_{11} - C_{12} > 0, \tag{9}$$

$$C_{44} > 0. \tag{10}$$

Young's modulus (E), Poisson's ratio (ρ), bulk modulus (B) and shear modulus (G) can be calculated by the following equations by using C_{11}, C_{12} and C_{44} elastic constants for cubic system [20–29]. In the present study, determination of the mechanical properties was carried out by using of elastic constants (C_{11}, C_{12} and C_{44}). Figure 15 shows the calculated Young's modulus (E), shear modulus (G) and bulk modulus (B) values. Highest Young's modulus was in the alloy-1, while lowest Young's modulus was in the alloy-3.

$$E = \frac{1}{5}(3C_{44} + C_{11} - C_{12}), \tag{11}$$

$$B = \frac{1}{3}(C_{11} + 2C_{12}), \tag{12}$$

$$G = \frac{C_{11} - C_{12} + 3C_{44}}{5}, \tag{13}$$

$$\rho = \frac{3B - 2G}{2(3B + G)}. \tag{14}$$

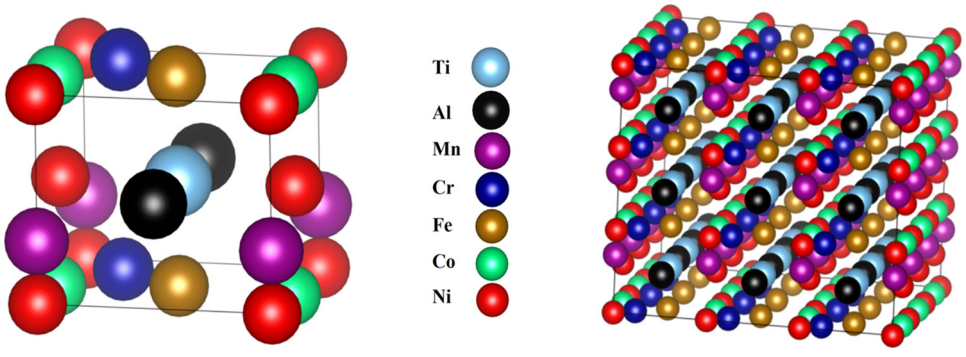

Figure 13. Unit cell (left), and superlattice (right).

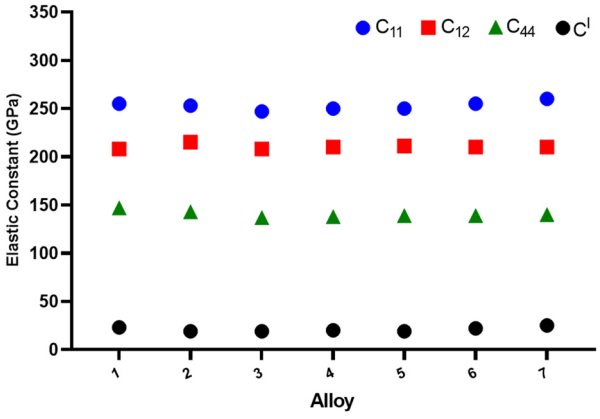

Figure 14. Elastic constants of the high entropy alloys.

Figure 16 shows the Poisson's ratio and *G*/*B* ratio (Pugh's ratio) values. Poisson's ratio (ρ) determines the shear deformation capacity of alloys. Increasing Poisson's ratio, increase the plastic deformation capacity and ductility. Ductile materials such as metals have Poisson ratio of 0.30–0.33. Brittle materials such as covalent materials have Poisson's ratio of 0.20–0.25, while ionic materials have Poisson's ratio of 0.10–0.15. As the Poisson's ratio values are 0.30–0.32, all alloys are ductile according to the Poisson's ratio values. *G*/*B* ratio is known as Pugh's ratio, which is depending on the brittle/ductile nature of metals and can be used for the characterization of ductility. If the Pugh's ratio is lower than 0.57, the alloy is ductile. If the Pugh's ratio is higher than 0.57, the alloy is brittle. As the Pugh's ratio values are about 0.40–0.45, all HESA are ductile. In the present study, mechanical properties were determined by experimental and first principles methods. Difference between the experimental and first principles elastic modulus was 5–20%. Difference was attributed to the presence of porosity and superlattice size used for calculations. Larger superlattice structures could not be calculated due to computer capacity.

Density of states (DOS) of the materials could be employed in order to determine the stability of the alloy with respect to their behaviour at the Fermi energy level (E_f). Material with the highest DOS at the Fermi energy level is the least stable. Figure 17 illustrates the energy values of the alloys at the Fermi level (E_f). Alloys with lower energy level are more stable. Increasing mixing entropy or mixing enthalpy values increased the energy value and decreased the stability of the alloys. Most stable alloy was alloy-2, while least stable alloys were alloy-4 and alloy-7.

3.2 Thermal properties

Figure 18 shows the effect of (a) heat treatment and (b) composition (alloy type) on the DSC curves of the specimens. DSC curves show the major phase transformations

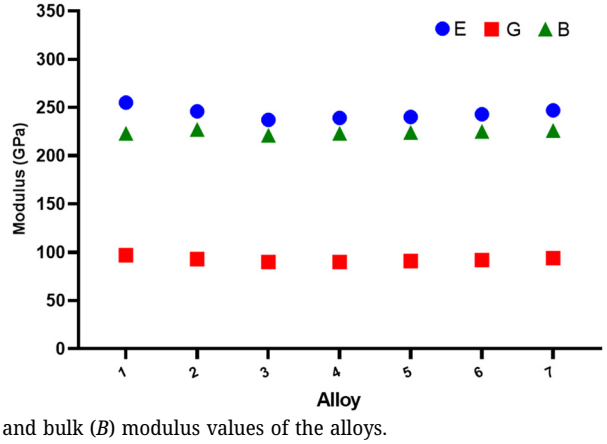

Figure 15. Young's (*E*), shear (*G*) and bulk (*B*) modulus values of the alloys.

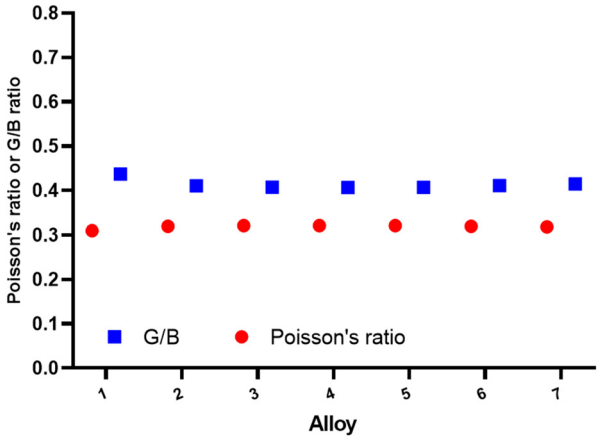

Figure 16. Poisson's ratio and *G*/*B* ratio values of the alloys.

of the HESA specimens. Precipitation hardening (aging) temperature increased the solvus temperature of the γ' precipitates. The first peaks at temperatures between 720 and 800°C shows the starting of the precipitation of γ'. Second peaks at about 910 and 950°C shows the dissolution of the γ' intermetallic precipitates. Melting temperature values of alloy 1 and alloy 2 were higher. Highest melting temperature was in te alloy 1, while lowest melting temperature was in alloy 7.

Traditional alloy design strategy depends on one principal element and addition of secondary minor elements. In the high entropy alloys, fundamental is to add five or more principal elements in equimolar ratios in order to increase the configuration entropy in order to produce a single-phase solid solution. Unfortunately, matrix of a high entropy alloy is not strong enough for elevated temperatures. The heat treatment in order to produce intermetallic precipitates consists of a solution treatment above the solvus temperature and precipitation hardening at lower temperatures in order to produce fine intermetallics. Elevated temperature strength of the superalloys depends on the amount and size of the γ^I precipitates. Strength of traditional alloys decreases with temperature. But, in the superalloys, strength increases with increasing temperature up to 750–800°C. For elevated temperatures, as the γ^I precipitates dissolves, the strength decreases [32–35]. There are two mechanisms for precipitation hardening of the metals by-pass of dislocations (Orowan theory) or shearing of dislocations mechanism [32–35].

3.3 Elevated temperature oxidation tests

Figure 19 shows the oxidation behaviour test results of the specimens at 900°C for different durations from 1 to 4 h in air atmosphere. Weight of the alloys was increased with the holding time in air at 900°C. As seen, weight gain values of the alloy-5, alloy-6 and alloy-7 were relatively

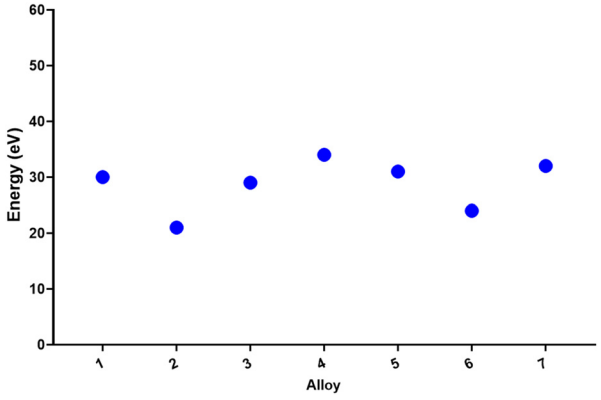

Figure 17. Energy values of the alloys at Fermi level.

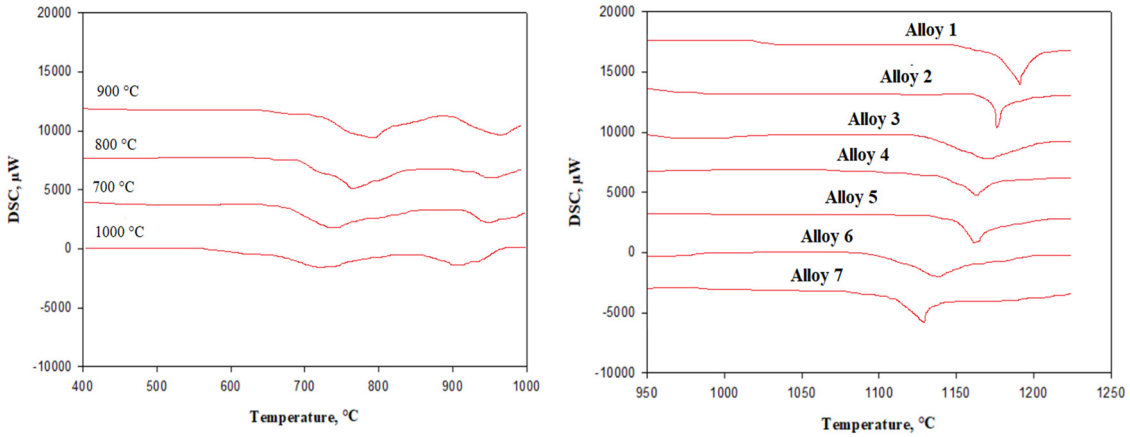

Figure 18. Effect of heat treatment (left), and composition on the DSC curves of the specimens (right).

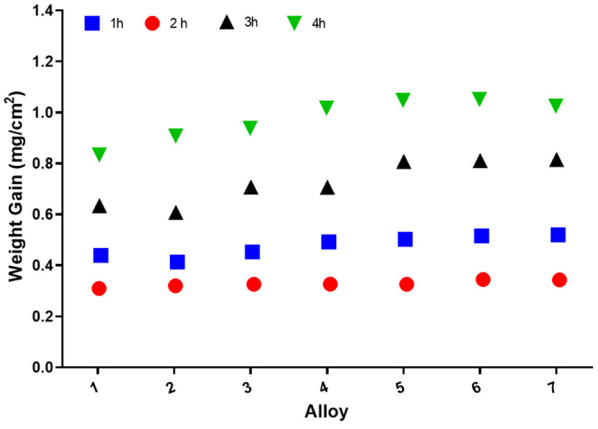

Figure 19. Oxidation results of the specimens at different durations.

higher. Increasing weight gain in the alloys was attributed to the decreasing Ni, Cr, and Co contents. Highest weight gain value was in the alloy-6, while lowest weight gain value was in the alloy-2.

3.4 Comparison with traditional Ni-based superalloys

Table 6 shows the density values and price values of the HESA. Table 6 also shows the density and price values of a traditional Ni-based superalloy (Inconel 718) for comparison. Mean cost values of the HESA were calculated by using price of alloying elements (Al is 2,800 US$ per tonne, Co is 4,3720 US$ per tonne, Cr is 7,400 US$ per tonne, Fe is 650 US$ per tonne, Mn is 1,800 US$ per tonne, Ni is 18,250 US$ per tonne, Ti is 8,000 US$ per tonne, Mo is 55,000 US$ per tonne, and Nb is 77,000 US$ per tonne). In addition, mean density values of the HESA were calculated by using density of alloying elements (Al is 2.71 g/cm^3, Co is 8.9 g/cm^3,

	Alloy	Cost (US $/tonne)	Density (g/cm^3)
(1)	$Al_{15}Co_9Cr_{16}Fe_{20}Mn_4Ni_{33}Ti_3$	12,003	7.29
(2)	$Al_{15}Co_4Cr_{16}Fe_{20}Mn_4Ni_{38}Ti_3$	10,729	7.29
(3)	$Al_{20}Co_4Cr_{16}Fe_{20}Mn_4Ni_{33}Ti_3$	9,957	6.98
(4)	$Al_{20}Co_9Cr_{16}Fe_{15}Mn_4Ni_{33}Ti_3$	12,110	7.04
(5)	$Al_{20}Co_9Cr_{11}Fe_{20}Mn_4Ni_{33}Ti_3$	11,773	7.07
(6)	$Al_{24}Co_6Cr_{11}Fe_{23}Mn_3Ni_{30}Ti_3$	10,027	6.80
(7)	$Al_{25}Co_5Cr_{10}Fe_{25}Mn_3Ni_{27}Ti_5$	9,170	6.65
Reference	Inconel 718 (NiCr19Fe19Nb5Mo3)	17,617	8.67

Table 6. Mean cost and density values of the HESA.

Cr is 7.19 g/cm^3, Fe is 7.87 g/cm^3, Mn is 7.47 g/cm^3, Ni is 8.9 g/cm^3, Ti is 4.5 g/cm^3, Mo is 10.22 g/cm^3, and Nb is 8.58 g/cm^3) [36,37]. As seen from the Table 6, cost values of the HESA were 32–48% lower than traditional Ni-based superalloy (Inconel 718). In addition, density values of the HESA were 16–23% lower than traditional superalloy (Inconel 718). Especially density and cost values of the alloy-7 ($Al_{25}Co_5Cr_{10}Fe_{25}Mn_3Ni_{27}Ti_5$) were 48 and 23% lower than the traditional Inconel 718 superalloy.

4. Conclusions

In this study, AlCoCrFeMnNiTi based refractory-free HESA were prepared by PIM for aviation applications. In addition, aging heat treatment was carried out in order to enhance the high temperature mechanical properties. MA includes material transfer (diffusion) in order to obtain a uniform alloy. Powder injection molding is a powder metal forming technology used for manufacturing of small-medium sizes complex products. Powder injection molding route includes feedstock preparation by blending metal powder and binder, granulation, powder injection molding, debinding, sintering steps.

The main conclusions of the present study are as follows:

(1) Al, Co, Cr, Fe, Mn, Ni, Ti elements were used in order to develop light, cheap HESA with creep and oxidation resistance.
(2) ΔS_{mix}, δ, VEC parameters of different compositions were calculated and compared. The optimum composition of the HESA was $Al_{15}Co_9Cr_{16}Fe_{20}Mn_4Ni_{33}Ti_3$ due to its optmimum ΔS_{mix}, δ, VEC parameters for solid solution fcc structure formation.
(3) For mechanical properties, 900°C was the optimum precipitation hardening temperature for the HESA.
(4) HESA consited of face centered cubic (γ) matrix phase and γ' precipitates. Some body centered cubic phase was also observed.
(5) Specimens were produced successfully without microcracks by using PIM method. There is grain-coarseing, and segregation in HESA and high entropy alloys produced by vacuum arc melting.
(6) Solution treatment and aging increased the corrosion rate of the as-sintered specimen. Maximum corrosion rate was obtained at 1,000°C aging. Corrosion rate value of the specimens aged at 800 and 900°C was close to corrosion rate of the solution treated specimen.
(7) Increasing aging temperature increased the solvus temperature of the γ' precipitates according to DSC analysis.
(8) All the alloys were mechanically stable according to their C', C_{11}, C_{12} and C_{44} elastic constants according to the first priciples based computational study.
(9) Highest Young's modulus was in the alloy-1, while lowest Young's modulus was in the alloy-3 according to the first priciples based computational study.
(10) All alloys were ductile according to their Poisson's ratio and G/B ratio values according to the first priciples based computational study.
(11) Most stable alloy was alloy-2, while least stable alloys were alloy-4 and alloy-7 accoridng to the DOS at the Fermi level (E_f) according to the first priciples study.
(12) Difference between the experimental and first principles elastic modulus values was 5–20%. Difference was attributed to the presence of porosity and superlattice size.
(13) Cost values of the HESA were calculated by using price of alloying elements. Cost values of the HESA were 32–48% lower than traditional Ni-based superalloy (Inconel 718).
(14) Density values of the HESA were calculated by using density of alloying elements. Density values of the HESA were 16–23% lower than traditional Ni-based superalloy (Inconel 718).

Acknowledgments

This work was supported partially by Scientific Research Projects Coordination Unit of Istanbul University-Cerrahpasa, Project Numbers of 36358, 35175.

Funding information

This work was supported partially by Scientific Research Projects Coordination Unit of Istanbul University-Cerrahpasa, Project Numbers of 36358, 35175.

Author contributions

Emre Atakan Meric: writing, methodology, investigation, Berke Soy: writing, methodology, investigation, Ilven Mutlu: conceptualization, writing – original draft, editing, supervision.

Conflict of interest statement

The authors declare that they have no any conflict of interest. This is an original work and it has not been submitted to any other journal for review.

Data availability statement

The data are available on request. The authors can share the data required to reproduce these findings by e-mail.

References

[1] Chen, Y.T., Chang, Y.J., Murakami, H., Gorsse, S., Yeh, A.C., Designing high entropy superalloys for elevated temperature application, Scr. Mater., 2020, 187: 177–182

[2] Whitfield, T.E., Stone, H.J., Jones, C.N., Jones, N.G., Microstructural degradation of the $AlMo_{0.5}NbTa_{0.5}TiZr$ refractory metal high-entropy superalloy at elevated temperatures, Entropy, 2021, 23(1): 80

[3] Yang, J.J., Kuo, C.M., Lin, P.T., Liu, H.C., Huang, C.Y., Yen, H.W., et al., Improvement in oxidation behavior of $Al_{0.2}Co_{1.5}CrFeNi_{1.5}Ti_{0.3}$ high-entropy superalloys by minor Nb addition, J. Alloy. Compd., 2020, 825: 15398

[4] Senkov, O.N., Jensenb, J.K., Pilchaka, A.L., Miracle, D.B., Fraser, H.L., Compositional variation effects on the microstructure and properties of a refractory high-entropy superalloy $AlMo_{0.5}NbTa_{0.5}TiZr$, Mater. Des., 2018, 139: 498–511

[5] Shafiee, A., Moon, J., Kim, H.S., Jahazi, M., Nili-Ahmadabadi, M., Precipitation behaviour and mechanical properties of a new wrought high entropy superalloy, Mater. Sci. Eng. A, 2019, 749: 271–280

[6] Yurchenko, N., Panina, E., Rogal, Ł., Shekhawat, L., Zherebtsov, S., Stepanov, N., Unique precipitations in a novel refractory Nb-Mo-Ti-Co high-entropy superalloy, Mater. Res. Lett., 2022, 10(2): 78–87

[7] Cai, Y., Liu, F., Tan, Y., Wang, L., Ji, X., Xiang, S., Synergy effect of multi-strengthening mechanisms in CoNiCr-based high-entropy superalloy at cryogenic temperature, Mater. Sci. Eng. A, 2024, 901: 146531

[8] Li, Y., Olejarz, A., Kurpaska, Ł., Lu, E., Alava, M.J., Kim, H.S., et al., Designing cobalt-free face-centered cubic high-entropy alloys: A strategy using d-orbital energy level, Int. J. Refract. Met. Hard Mater., 2024, 124: 106834

[9] Chen, R., Qin, G., Zheng, H., Wang, L., Su, Y., Chiu, Y., et al., Composition design of high entropy alloys using the valence electron concentration to balance strength and ductility, Acta Mater., 2018, 144: 129e137

[10] Momeni, V., Hufnagl, M., Shahroodi, Z., Gonzalez-Gutierrez, J., Schuschnigg, S., Kukla, C., et al., Research progress on low-pressure powder injection molding, Materials, 2023, 16: 379

[11] Dehghan-Manshadi, A., Yu, P., Dargusch, M., StJohn, D., Qian, M., Metal injection moulding of surgical tools, biomaterials and medical devices: A review, Powder Technol., 2020, 364: 189–204

[12] Aslam, M., Ahmad, F., Binti, P.S.M., Yusoff, M., Altafa, K., Omar, M.A., et al., Powder injection molding of biocompatible stainless steel biodevices, Powder Technol., 2016, 295: 84–95

[13] Won Lee, D., Shin, D.S., Ha, H., Park, S.J., Lee, K.A., Kim, H.S., Modulated heating rate effect on optimizing sintered density and microstructure in CoCrFeMnNi high-entropy alloy fabricated through metal injection molding, Mater. Charact., 2024, 214: 114037

[14] Meza, A., Barbosa, A., Tabares, E., Torralba, J.M., Tailoring high-entropy alloys via commodity powders for metal injection moulding: A feasibility study, J. Mater. Res. Technol., 2024, 31: 109–116

[15] Kang, B., Kong, T., Ryu, H.J., Hong, S.H., The outstanding tensile strength of Ni-rich high entropy superalloy fabricated by powder metallurgical process, Mater. Chem. Phys., 2019, 235: 121749

[16] Suryanarayana, C., Mechanical alloying and milling, Prog. Mater. Sci., 2001, 46(1): 184

[17] Suryanarayana, C., Mechanical alloying: A critical review, Mater. Res. Lett., 2022, 10(10): 619–647

[18] Miracle, D.B., Senkov, O.N., A critical review of high entropy alloys and related concepts, Acta Mater., 2017, 122: 448–511

[19] Cantor, B., Multicomponent high-entropy Cantor alloys, Prog. Mater. Sci., 2021, 120: 100754

[20] Segall, M.D., Lindan, P.J., Probert, M.A., Pickard, C.J., Hasnip, P.J., Clark, S.J., et al., First-principles simulation: ideas, illustrations and the CASTEPcode, J. Phys. Cond. Matter., 2002, 14: 2717–2744

[21] Clark, S.J., Segall, M.D., Pickard, C.J., Hasnip, P.J., Probert, M.I., Refson, K., et al., First principles methods using CASTEP, Z. Kristallogr.-Cryst. Mater., 2005, 220: 567–570

[22] Chen, H.L., Lin, L., Mao, P.L., Liu, Z., Phase stability, electronic, elastic and thermodynamic properties of Al-RE intermetallics in Mg-Al-RE alloy: A first principles study, J. Magnes. Alloy., 2015, 3: 197–202

[23] Sahara, R., Emura, S., Tsuchiya, K., Theoretical investigation of effect of alloying elements on phase stability in body-centered cubic Ti-X alloys (X= V, Cr, Fe, Co, Nb, and Mo), J. Alloy. Compd., 2015, 634: 193–199

[24] Mao, P., Yu, B., Liu, Z., Wang, F., Ju, Y., First-principles calculations of structural, elastic and electronic

properties of AB2 type intermetallics in Mg–Zn–Ca–Cu alloy, J. Magnes. Alloy., 2013, 1: 256–262

[25] Lozynskyi, V., Trembach, B., Hossain, M.M., Kabir, M.H., Silchenko, Y., Krbata, M., et al., Prediction of phase composition and mechanical properties Fe–Cr–C–B–Ti–Cu hardfacing alloys: Modeling and experimental Validations, Heliyon, 2024, 10: e25199

[26] Shitara, K., Yokota, K., Yoshiya, M., Umeda, J., Kondoh, K., First-principles design and experimental validation of β-Ti alloys with high solid-solution strengthening and low elasticities, Mater. Sci. Eng. A, 2022, 843: 143053

[27] Wang, Z.P., Fang, Q.H., Li, J., Liu, B., First-principles predictions of structural, mechanical and electronic properties of βTiNb under high pressure, Superlattices Microstruct., 2018, 116: 141–150

[28] Jiang, D.Y., Ouyang, C.Y., Liu, S.Q., Mechanical properties of W–Ti alloys from first-principles calculations, Fusion Eng. Des., 2016, 106: 34–39

[29] Wu, Z., Malmir, H., Benafan, O., Lawson, J.W., Predicting the martensitic transition temperatures in ternary shape memory alloys $Ni_{0.5}Ti_{0.5}$– xHfx from first principles, Acta Mater., 2023, 261: 119362

[30] Mutlu, I., Ekinci, S., Oktay, E., Characterization of heat treated titanium-based implants by nondestructive eddy current and ultrasonic tests, J. Mater. Eng. Perform., 2014, 238(6): 2083–2091

[31] German, R., Bose, M.A., Injection molding of metals and ceramics, metal powder industries federation, Vol. 105, College Road East Princeton, New Jersey, 1997

[32] Chen, J., Zhou, X., Wang, W., Liu, B., Lv, Y., Yang, W., et al., A review on fundamental of high entropy alloys with promising high temperature properties, J. Alloy. Compd., 2018, 760: 15e30

[33] Antonov, S., Detrois, M., Tin, S., Design of novel precipitate-strengthened Al-Co-Cr-Fe-Nb-Ni high-entropy superalloys, Metall. Mater. Trans. A, 2018, 49A: 305

[34] He, J.Y., Wang, H., Huang, H.L., Xu, X.D., Chen, M.W., Wu, Y., et al., A precipitation-hardened high-entropy alloy with outstanding tensile properties, Acta Mater., 2016, 102: 187–196

[35] Eißmann, N., Mühle, U., Gaitzsch, U., Walther, G., Weißgärber, T., Kieback, B., Precipitation hardening of high entropy alloy CoCrFeMnNi containing titanium, J. Alloy. Compd., 2021, 857: 157610

[36] https://www.metal.com/

[37] https://www.lme.com/